Accurate density functional calculations for the phonon dispersion relations of graphite layer and carbon nanotubes

O. Dubay and G. Kresse

Institut für Materialphysik, Universität Wien and Center for Computational Material Science, Sensengasse 8, A-1090 Wien, Austria

(Received 10 June 2002; revised manuscript received 27 September 2002; published 6 January 2003)

Accurate calculations for the phonon dispersion relations of single-wall armchair and zigzag nanotubes are presented. The calculations are performed using a plane-wave basis set and density functional theory. To ensure the accuracy of the presented calculations, the phonon dispersion relation of an isolated graphite layer is calculated and the results are compared to experiment. Errors are small, but some notable discrepancies between experiment and theory are observed and discussed. For armchair and zigzag nanotubes the dependence of Raman-active and infrared-active modes on the radius is investigated in detail concentrating on the modes in the *G* band. The results are compared to those predicted by the zone-folding method using the calculated force constants for graphite. We find a general softening of most high-frequency modes and a substantial lowering of one particular longitudinal A_1 mode in metallic tubes. We associate this mode with the Breit-Wigner-Fano lines observed usually in metallic tubes. The precise electronic mechanism leading to the softening of the longitudinal A_1 mode is discussed in detail.

DOI: 10.1103/PhysRevB.67.035401 PACS number(s): 63.22.+m, 63.20.Dj, 63.20.Kr, 71.15.Mb

I. INTRODUCTION

Since the discovery of carbon nanotubes,[1] much attention has been devoted to the investigation of their vibrational properties, experimentally as well as theoretically. Among other things, the vibrational spectra are useful for the characterization or identification of different nanotubes in experimental samples. Theoretically, zone-folding techniques were used initially for an approximate evaluation of the vibrational spectra of carbon nanotubes. Although this approach yields a good qualitative understanding of many properties,[2–8] it also has several shortcomings. First, the force constants (FC's) are usually fitted to the experimentally observed phonon dispersion relation of graphite.[2–8] Any inaccuracy in the experiment will therefore affect the accuracy of the predicted frequencies. This problem is particularly severe for low-frequency modes, corresponding to the elastic regime. Additionally, the zone-folding approach neglects curvature effects, and finally the force constants are usually chosen in a very restrictive manner, for instance, such that the full Hessian is the sum of two-atom Hessians, where these two-atom Hessians are diagonal in a coordinate frame which axes are formed by (i) the line connecting the two atoms, (ii) a normal to the graphene plane (graphene=one sheet of graphite), and (iii) a vector orthogonal to (i) and (ii).[2,3,8]

Valence force fields are more general than the zone-folding method, since they allow nonharmonic potential energy surfaces and bending forces. In Ref. 9 the valence force field model was used with a force field fitted to experimental data.[10,11] But it is again questionable whether curvature effects (which are not directly included in the fitting data base) are correctly accounted for, and the correct description of elastic modes is also not necessarily guaranteed.

A completely different route is taken in tight-binding (TB) and *ab initio* density functional calculations. In the latter, experiments only serve as a test database, but they are not directly used in the determination of the vibrational properties of nanotubes. Compared to *ab initio* methods, TB methods are faster and offer the possibility to treat much larger systems.[12–17] But *ab initio* methods are superior in terms of their predictive capabilities. It has been shown that the phonon dispersion relations of diamond and graphite can be predicted within a few percent accuracy.[18,19] Such methods have been used for nanotubes, but presently always in a rather approximate fashion: in Ref. 20, for instance, a local basis set method was used for the evaluation of the phonon spectrum of selected tubes. Although these calculations amply demonstrate the feasibility of large-scale first-principles calculations for carbon nanotubes, issues like basis set completeness and accuracy of *k*-point sampling remain to be addressed. This is exemplified by the observation that a minimal sp^3 basis set was applied in Ref. 20, and as a result of this approximation, the frequencies of the high-frequency optical bands were overestimated by approximately 100 cm^{-1} compared to the experiments.[10,11,21]

Plane-wave calculations are in that respect superior and more reliable. For the radial breathing mode, such calculations were reported in Ref. 22, and the aim of this work is to extend these calculations to the full phonon dispersion relations of carbon nanotubes. We also tried to make our calculations technically as precise as possible (*k*-point sampling, basis sets), so that our results are essentially exact in the limits established by the local density approximation. To achieve this aim, we first calculated the force constants and the phonon dispersion relation of a single graphite layer (Sec. II B). At this step extensive tests with respect to the electron-ion potential and with respect to the *k*-point sampling were performed. These calculations also yield a well-founded set of force constants for graphene that can be used for the prediction of the dispersion relations of nanotubes using the zone-folding technique. In Sec. III C, we present these phonon dispersion relations for (n,n) armchair and

$(n,0)$ zigzag tubes for $n=9-11$ and $n=7-18$, respectively, and compare them with exact frozen phonon density functional calculations. This allows to access how curvature affects the frequencies. We find a general softening of most high-frequency modes and a substantial lowering of one particular longitudinal A_1 mode in metallic tubes. As discussed in our recent work, we associate this mode with the Breit-Wigner-Fano lines observed with Raman spectroscopy in metallic tubes.[23] The electronic mechanism that leads to this softening is discussed in detail in Sec. IV. We finish with our conclusions in Sec. V.

II. METHODOLOGY

A. First-principles calculations

Our first-principles calculations are based on density functional theory (DFT) in the local density approximation (LDA) (see, e.g., Refs. 24 and 25) and employ a plane-wave basis set.[26,27] As in our previous work (see Ref. 22) we use the Vienna *ab initio* simulation package (VASP),[28,29] where in the most recent version the interaction between the ions and electrons is described by the projector augmented-wave[30] (PAW) method in the implementation of Kresse and Joubert.[31] The projector augmented-wave method uses the exact valence wave functions instead of nodeless pseudo wave functions usually applied in the context of pseudopotential calculations. This improves the transferability and reliability of the potentials.

In the present PAW potentials, the $2s$ and $2p$ orbitals are treated as valence orbitals and two partial waves are used for any s and p orbitals. Two carbon potentials were used in the present work: (i) a hard potential with a radial cutoff of 1.2 a.u. and 1.5 a.u. for the s and p partial waves, respectively, and (ii) a soft potential with a radial cutoff of 1.5 a.u. for the s and 1.85 a.u. for the p partial waves. The hard potential yields accurate results at a plane-wave cutoff of 400 eV, whereas the soft potential gives reliable results already at a plane-wave cutoff of 250 eV. It will be demonstrated that the soft potential leads to reliable results for the vibration frequencies (Table I), and therefore most of the calculations presented here were performed with the soft potential.

B. Phonon dispersion relation of graphene

We first optimized the lattice constant of a single graphite layer and obtained a value of $a=2.458$ Å. This corresponds to a carbon-carbon distance of $a_{CC}=1.419$ Å, which is identical to the experimental value of Ref. 32. For the calculation of the force constants of the graphite layer, a parallelogram-shaped supercell containing 128 atoms was used. The graphite layers were separated by 8 Å vacuum. Five irreducible Γ-centered k points were used to sample the Brillouin zone (corresponding to a 24×24 Monkhorst-Pack k-point grid in the Brillouin zone of the primitive cell). It must be emphasized that such a dense k-point set is required to reduce the errors to a fraction of a percent. We used a smearing width of 0.6 eV,[33] but tests indicate that the results for graphene are fairly insensitive to the width of the smearing function.

TABLE I. Comparison of experimental and calculated frequencies of a graphite sheet at the Γ and M points. Values for "soft PAW" and "hard PAW" are the results of calculations with the two different potentials. All values are in cm^{-1}.

	Soft PAW	Hard PAW	Experiment
Γ	890	896	868 [a]
	1595	1597	1582, [b]1587 [c]
M	475	476	
	618	627	
	636	641	
	1339	1347	
	1380	1373	
	1442	1434	

[a]Reference 35.
[b]$\omega(E_{2g_2})$, Refs. 35–37.
[c]$\omega(E_{1u})$, Refs. 35 and 38.

For calculating the force constants central differences were used. One carbon atom was displaced into two directions: one in plane and one orthogonal to the plane of the graphite layer. The displacement length was 0.03 Å in both cases. The full Hessian matrix was constructed by using the symmetry of the graphite layer.

C. Nanotubes

The nanotubes were placed into square-shaped cells, so that neighboring tubes were separated by a 9 Å vacuum. The initial geometry was constructed using the interatomic distance as obtained for graphene.

The geometry of the nanotubes was optimized before performing the FC calculations. In the case of zigzag tubes, the tube radius and the z coordinate (coordinate parallel to the tube main axis) were optimized simultaneously. The height of the tube supercell was not optimized, but test calculations on narrow tubes show that the difference between the used height and the optimal height is less than 1%.

In the case of armchair tubes, it turned out that optimizing the radius was sufficient for reducing the forces to a reasonably small value. For armchairs the resulting forces were smaller than 0.08 eV/Å per atom, and for zigzag tubes the forces were less than 0.04 eV/Å per atom after geometry optimization.

The FC calculations were done using central finite differences. For calculating the Γ-point frequencies, we used the elementary cell only. For the phonon dispersions of selected tubes [(10,10) and (10,0)] supercells containing four elementary cells were applied.

To derive all force constants, it is sufficient to displace a single atom into three orthogonal directions: parallel to the tube axis (z), towards the center of the tube (x), and parallel to the tube surface (y). The displacement was 0.03 Å, and we used positive and negative displacements for each direction. The complete set of force constants was calculated applying the symmetry of the tube. A reasonable calculational setup was determined by performing extensive test calcula-

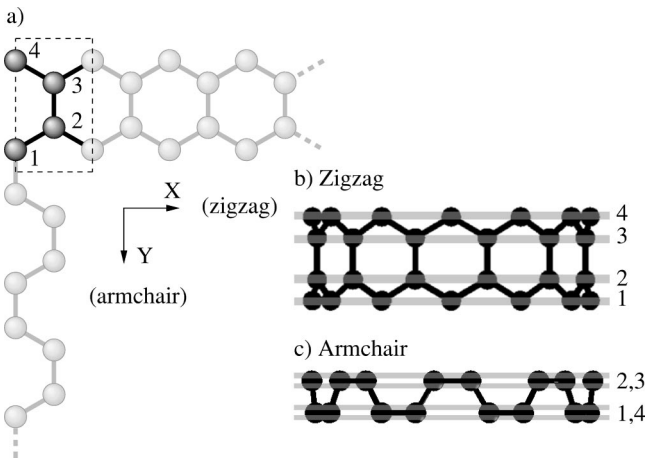

FIG. 1. Creation of the unit cell of armchair and zigzag nanotubes. Dashed box in (a) contains a four-atom graphite unit cell, which can be replicated and rolled up in either the *X* or *Y* direction to form the (b) zigzag or (c) armchair unit cell. The gray stripes in (b) and (c) show the rings formed by atoms 1–4.

tions on several tubes [(4,4), (8,0), and (12,0)] and also a rectangular graphene supercell corresponding to a zigzag tube (14,0). We decided to use 13 irreducible k points for semiconducting zigzag tubes, 33 irreducible k points for metallic zigzag tubes, and 57 irreducible k points for armchair tubes. The k points in reciprocal coordinates were $(0,0,n/24)2\pi/a_z$, $n=0,1,2,\ldots,12$, for semiconducting zigzag tubes, $(0,0,n/64)2\pi/a_z$, $n=0,1,2,\ldots,32$, for metallic zigzag tubes, and $(0,0,n/112)2\pi/a_z$, $n=0,1,2,\ldots,57$, for (metallic) armchair tubes. We had to use these dense k-point grids in order to describe the electronic states around the Fermi energy correctly. Although most phonon modes are rather insensitive to the k-point sampling, one particular mode couples strongly to the electronic states at the Fermi energy and changes significantly when the number of k points is reduced. Hence, when we tried to reduce the k-point grids, substantial errors were found for this particular mode (see Sec. IV). Even with this fine-grained sampling, the eigenvalue spectrum remains rather coarse around the Fermi level, and this in turn can lead to errors in the determination of the Fermi energy. To reduce these errors the eigenstates were broadened (smeared) using a scheme devised by Methfessel and Paxton.[33] For the metallic tubes, the parameters $\sigma=0.1$ eV and $N=1$ were used throughout the calculations since tests indicate that this yields a reasonable description of the electronic density of states close to the Fermi energy and to accurate interatomic force constants. Test calculations with twice as many k points and half the smearing width σ changed the frequencies by at most 5 cm^{-1}. It is estimated that this is the typical accuracy of our present calculations.

D. Symmetry classification of modes in nanotubes

To discuss the differences between zone-folding and exact *ab initio* calculations in more detail, we characterized the modes at Γ according to the symmetry of the nanotubes (D_{nd} or D_{nh}). In this section we briefly recapitulate the issues regarding symmetry, focusing on zigzag and armchair tubes.[3–6,15,34]

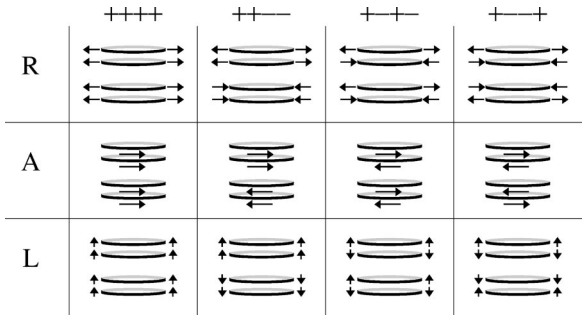

FIG. 2. Displacement patterns for the *A* modes of zigzag and armchair tubes. Arrows show (i) change of the radius in the first row (R), (ii) rotation in the second row (A), and (iii) translation in the direction of the tube axis in the third row (L).

Armchair and zigzag tubes can be built starting from a rectangular four atom graphite supercell (Fig. 1) instead of the usual parallelogram-shaped two-atom primitive cell. By replicating the rectangular unit cell n times along the shorter or the longer side and rolling it up to form a cylinder one obtains the unit cell of $(n,0)$ zigzag or (n,n) armchair tubes. The primitive cell of the nanotube can also be described by four coaxial rings with a common radius r [compare Figs. 1(b) and 1(c)]. By means of this construction, the symmetry group of $(n,0)$ and (n,n) tubes always contains the D_n group as a subgroup. Since infinitely long armchair (n,n) and zigzag $(n,0)$ tubes also have an inversion center, they have $D_n \otimes i$ symmetry, where i represents the group of the tube inversion symmetry.[3,5]

At the Γ point, vibrational modes of $(n,0)$ and (n,n) tubes can be classified according to the irreducible representation to (i) 12 A modes, (ii) 12 (doubly degenerated) E_k modes, where k is an integer $1 \leqslant k < n/2$, and, optionally, (iii) 6 doubly degenerated B modes for even n. The modes can be further characterized by their behavior with respect to inversion and the twofold axis for rotation (C_2'). As follows from group theory,[34] the A_{2u} and E_{1u} modes are infrared active, while A_{1g}, E_{1g}, and E_{2g} are Raman active. All other modes are silent.

For achiral nanotubes, the displacement patterns can be envisaged in a simple manner: for A modes all atoms on one of the rings illustrated in Fig. 1 move in phase, either parallel to the tube axis (z) or radial (perpendicular to the tube axis) or axial (parallel to the ring). In zone folding, the vibrational frequencies of these modes are identical to the frequency at the Γ and M points of the graphene sheet.[3–6,34] Figure 2 illustrates the corresponding displacement patterns for such modes. For B modes, two neighboring atoms on one ring move in exactly the opposite direction.

All remaining modes are standing waves on the rings [Figs. 1(b) and 1(c)] or on the lines (in zone folding, Fig. 3), which follow the same pattern as A modes. They are denoted as E_n, where $2n$ is the number of nodes of the wave. (A modes can be considered as waves with zero nodes.) B modes can also be regarded as standing waves, where n equals the number of atoms in the ring; i.e., the number of nodes is the same as the number of atoms in the ring. Since

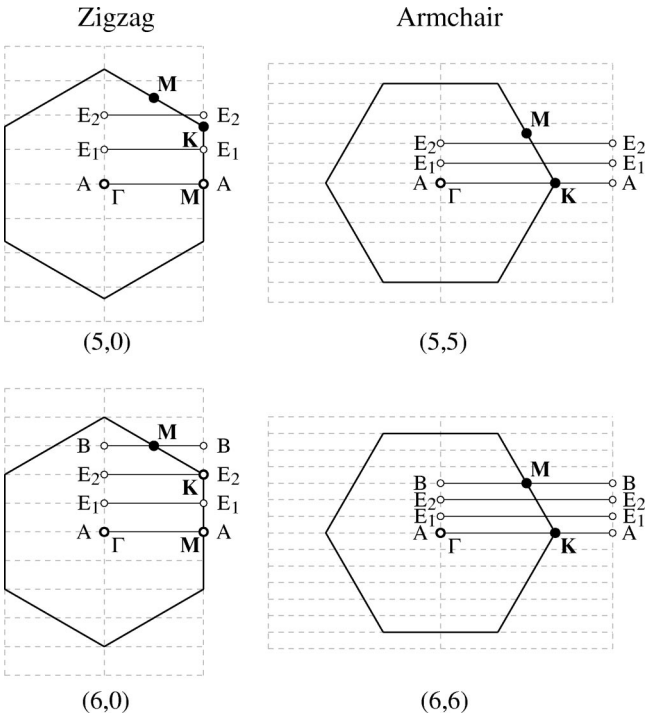

FIG. 3. Zone folding in zigzag [(5,0), (6,0)] and armchair [(5,5), (6,6)] tubes. The hexagons indicate the Brillouin zone of a graphite layer. Solid horizontal lines map to the line Γ,Z in the nanotube. Points that map to Γ in the nanotube are indicated with open circles and labeled according to the symmetry the corresponding phonons will have in the nanotube. Gray dashed lines are guidelines to the eye.

the waves must be closed, *B* modes are only present in $(n,0)$ and (n,n) tubes with even n. In zone folding, the *B* modes correspond to the ends of the lines crossing the *M* point (see Fig. 3). Note that the ends of these lines map to equivalent points of the graphene Brillouin zone; thus the *B* modes are doubly degenerated for zigzag and armchair tubes.

An important result of these simple arguments is that (i) *A* modes do not show a radius dependency in zone folding and (ii) there are 12 classes of phonon modes in achiral tubes, one for each *A* mode (Fig. 2); (iii) each *E* mode corresponds to a certain *A* mode, and the difference of their respective frequencies goes towards zero for increasing diameters.

III. RESULTS

A. Graphite

The phonon dispersion relation of a single graphite layer is shown in Fig. 4, together with a comparison with experiment.[11,21] Results for the Γ and *M* point are also shown in Table I. For the graphite layer we tested two different PAW potentials. The first one (hard) is more accurate but requires a plane-wave cutoff of 400 eV, whereas the second one (soft) yields converged results already at a plane-wave cutoff of 250 eV. In our test calculations we found that both potentials yield almost identical phonon frequencies at the Γ and *M* point (Table I) and hence we decided to use the soft potential for the remainder of this work.

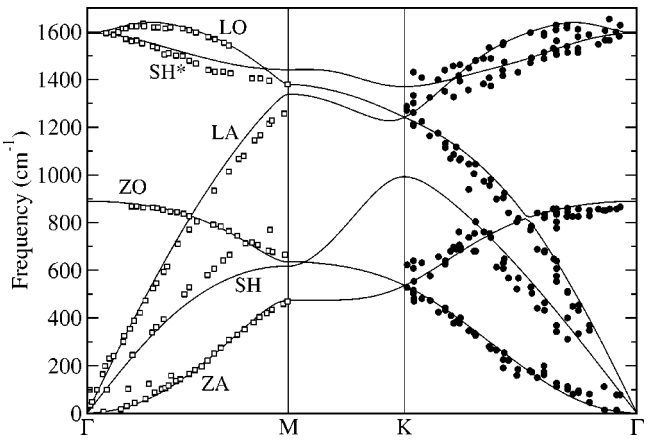

FIG. 4. Phonon dispersion relation of the graphene sheet. The solid lines show the results of the *ab initio* force constant approach for the soft potential. The open squares represent the reflection electron-energy-loss spectroscopy (REELS) data of Oshima *et al.* (Ref. 21) and the solid circles correspond to the high-resolution electron-energy-loss spectroscopy (HREELS) data of Siebentritt *et al.* (Ref. 11).

We also tested the sensitivity of the phonon dispersion relation to the magnitude of the displacement used in the finite differences. Larger displacements make the results less prone to numerical noise, which is present in the forces, because the electronic ground state is only determined with finite precision. But they can spoil the accuracy due to the anharmonicity of the forces. We have found that the displacement can be enlarged from 0.03 Å to 0.05 Å without a noticeable change of the phonon frequencies, if central differences are used.

To evaluate the accuracy of our vibrational frequencies, we compare the calculated dispersion relation with experiments for graphite (Fig. 4). It is first noted that modes corresponding to a movement of graphite planes with respect to each other are of course not correctly described by the present calculations, since only a single isolated graphite layer is investigated here. This concerns mainly the experimental branch with a frequency of 100 cm^{-1} at the Γ point. But other frequencies are hardly affected by the interaction between graphite planes, as a comparison of the present phonon dispersion relation with previous calculations for bulk graphite shows (see in particular Ref. 19). For the remaining branches the current calculations are more precise than those presented in Ref. 19, since longer-ranged force constants in the graphite plane were considered. Table I shows that our frequencies agree well with the measured Raman modes, although the *G* mode at 1595 cm^{-1} lies roughly 10 cm^{-1} too high. With the present PAW potential and similar *k*-point densities, calculations for bulk *graphite* yield a frequency of 1600 cm^{-1} for the *G* mode, suggesting that DFT gives the same frequency for the *G* mode in graphite and graphene.

For the dispersion relation, the agreement between theory and experiment is generally also very good (Fig. 4). Along Γ-*K* our results agree with experiment within the experimental error bars (see scatter of experimental data).[11] The comparison along Γ-*M* reveals larger discrepancies. At *M*, the frequency of the shear horizontal (SH) mode is significantly

lower than in the experiment. On the other hand, the longitudinal acoustic (LA) mode lies above the experimental values. We note that other first-principles calculations are in general agreement with our results,[19,20,39] which indicates that we either observe one of the cases, where density functional theory fails to predict the correct dispersion relation, or that the experimental data are not completely reliable along Γ-M.

Finally, we note that the longitudinal optic (LO) mode shows the characteristic overbending also observed in the experiment. The overbending is so strong that the LO mode lies below the SH* mode at the M point. This behavior is in agreement with all published first-principles calculations,[19,20,39] but presently, the experimental data for the LO mode are too scarce close to M to allow validation of this theoretical result. We note that force constants are usually fitted with the assumption that the LO and SH* modes do not cross along Γ-M.

B. Force constants for graphene

Table II shows the force constants for a graphite layer as derived from our first-principles calculations. The force constants decay fairly rapidly. At the 15th neighbor they are reduced by at least a factor of 300 and 4000 compared to the nearest neighbor for in plane (x,y) and out of plane (z), respectively. The table includes two sets of force constants, which are redundant due to inversion symmetry (atoms number 5 and 5′ and atoms number 10 and 10′). Note that the neighbors 20 and 20′ are not redundant in this manner. The discrepancies for the two redundant sets give an estimation for the numerical reliability of the tabulated constants (compare respective columns with radial derivatives). The discrepancy between these two set is at most 0.0005 eV/Å, which is a factor of 10 000 smaller than the force constant for the nearest neighbor and about 100 times smaller than the force constant at the 14th neighbor, indicating that the precision of the present calculation is indeed sufficient. It is, however, important to emphasis that even very small errors in the force constants can have a substantial effect on low-frequency modes. From the approximate errors and a simple error analysis we can estimate that high-frequency modes are correct to within $0.3\ \mathrm{cm}^{-1}$ and frequencies around $200\ \mathrm{cm}^{-1}$ are correct to within $2\ \mathrm{cm}^{-1}$, but very-low-frequency modes (20–$50\ \mathrm{cm}^{-1}$) might be wrong by up to $10\ \mathrm{cm}^{-1}$.

It would be interesting to compare our force constants to those fitted to experimental data, but unfortunately, the values even for the first neighbor differ already by up to 30%. We also note that the common assumption that the force constant matrix is diagonal in a basis spanned by the vector connecting the two atoms (radial part) and the orthogonal vector (angular part) is not fulfilled, e.g., for the second and fourth neighbors.

Though the force constants decay reasonably, it is not possible to restrict them to a small number of neighbors without losing accuracy. Neglecting the force constants before the 20th neighbor causes significant changes in either the low- or high-frequency regions. The differences in phonon dispersion resulting from the use of 20 to 23 (all) neighbors are negligible.

As an additional test for the reliability of the truncated force constant matrix, we calculated the elastic stiffness. To this end, the stiffness s was first independently calculated by straining the graphene sheet either parallel to the x or y direction (see Fig. 5) by $1\pm\epsilon$ ($\epsilon=0.00,\ 0.01,\ 0.02$) and fitting the energy with a quadratic curve

$$E=E_0+\frac{s}{2}\epsilon^2 \quad \left(s=\frac{\partial^2 E}{\partial \epsilon^2}\right). \tag{1}$$

Due to the threefold symmetry, an isotropic value is expected and we found this indeed confirmed ($s=61$ eV/atom). The elastic stiffness can be calculated also by summing the interatomic force constants

$$\frac{1}{2}\sum_{i,j=1,2,3}^{\alpha,\beta}[\vec{R}(\alpha\beta)\hat{q}]\hat{q}_i D_{ij}(\alpha\beta)\hat{q}_j[\vec{R}(\alpha\beta)\hat{q}], \tag{2}$$

where $\hat{q}$ is a unit vector either parallel to x or y. $D_{ij}(\alpha\beta)$ are the Cartesian components of the interatomic force constant matrix between atoms α and β, and $\vec{R}(\alpha\beta)$ is the vector connecting atoms α and β. The index α runs over all atoms in the primitive cell and β over the entire interaction range. The summation gives a value of $s=63$ eV/atom. We emphasize that this value is very sensitive to the point of truncation, since force constants enter quadratically with the distance in Eq. (2). Hence, the small deviation from the more precise value calculated by straining the graphene sheet is acceptable. The experimental value for the elastic stiffness can be estimated from the value of the elastic constant of graphite, $c_{11}=1.06$ TPa, and the experimental lattice constants of graphite, $a_0=2.462$ Å, $c_0=6.707$ Å, yielding a value of $V_0\times c_{11}=58.2$ eV/atom,[40] which is in excellent agreement with the elastic stiffness calculate from the strained graphene sheet, demonstrating the accuracy of our density functional calculations. Sound velocities are also related to elastic constants. For simplicity we calculated them from the slope of acoustic branches (Fig. 4) and found values of 16 km/s and 26 km/s for the transversal acoustic (TA) and LA modes. This is in good agreement with the sound velocities extracted from experimental data (14 and $\approx$24 km/s).[20,21]

C. Nanotubes

The phonon dispersion relations of the (10,10) and (10,0) tubes were calculated exactly by means of large supercells containing an isolated nanotube, as explained in Sec. II C (4 times replicated elementary cells, i.e., 160 atoms for both tubes). The k-point mesh was correspondingly reduced by a factor of 4 compared to the values specified in Sec. II C. Figure 6 shows a comparison of these exact *ab initio* calculations with zone-folding results for the tubes (10,10) and (10,0). For zone folding, we used the force constants derived from the *ab initio* calculations for the flat sheet as calculated in the previous section. Since we use one consistent poten-

TABLE II. Interatomic force constants (eV/Å^2) for graphite between atom 0 and n as calculated by first principles (numbering scheme and axis are shown in Fig. 5). Second derivatives of the energy E are given with respect to the coordinates x, y, and z and also with respect to the longitudinal (l) and transversal (t) directions. Longitudinal is the direction parallel to the connection of the two atoms, and transversal is parallel to the layer plane and perpendicular to the longitudinal direction.

n	$\begin{pmatrix}\partial_{x_0}\partial_{x_n} & \partial_{x_0}\partial_{y_n}\\ \partial_{y_0}\partial_{x_n} & \partial_{y_0}\partial_{y_n}\end{pmatrix}$	$\begin{pmatrix}\partial_{r_0}\partial_{r_n} & \partial_{r_0}\partial_{t_n}\\ \partial_{t_0}\partial_{r_n} & \partial_{t_0}\partial_{t_n}\end{pmatrix}$	$\partial_{z_0}\partial_{z_n}$
1	+10.2054 +0.0000 +0.0000 +27.3244	+27.3244 +0.0000 +0.0000 +10.2054	+6.3182
2	−0.7888 +3.4419 +2.8814 +2.8600	+4.6859 −0.2811 +0.2794 −2.6147	−0.5063
3	−0.1210 −1.2247 −1.2247 +1.2931	−0.8281 −0.0000 −0.0000 +2.0002	+0.4160
4	+0.5662 +0.3115 +0.3116 −0.7382	−0.4057 −0.6482 −0.6483 +0.2337	−0.4943
5	+0.1064 +0.0000 +0.0000 +0.5238	+0.5238 +0.0000 +0.0000 +0.1064	+0.0693
5’	+0.4188 +0.1807 +0.1807 +0.2102	+0.5231 +0.0000 +0.0000 +0.1059	+0.0695
6	−0.1777 +0.1593 +0.1730 +0.0144	+0.1103 +0.0070 −0.0067 −0.2736	−0.0118
7	+0.0769 −0.1758 −0.1760 −0.1217	−0.1944 −0.1061 −0.1059 +0.1496	−0.0083
8	+0.0129 +0.0000 +0.0000 −0.4507	−0.4507 +0.0000 +0.0000 +0.0129	+0.0644
9	+0.0400 −0.0463 −0.0462 +0.0422	+0.0081 +0.0325 +0.0324 +0.0741	+0.0259
10	−0.0015 +0.1908 −0.0149 +0.0603	+0.1120 −0.0597 +0.1460 −0.0532	−0.0065
10’	−0.0313 +0.1735 −0.0321 +0.0900	+0.1119 −0.1459 +0.0597 −0.0532	−0.0065
11	−0.0335 −0.0920 −0.0920 +0.0728	−0.0866 +0.0000 +0.0000 +0.1259	+0.0019
12	+0.0201 +0.0048 +0.0436 +0.0479	+0.0619 +0.0193 −0.0195 +0.0061	+0.0013
13	−0.0033 −0.0018 −0.0018 −0.0495	−0.0315 −0.0226 −0.0226 −0.0213	−0.0041
14	−0.0088 +0.0237 +0.0238 −0.0854	−0.0762 −0.0343 −0.0344 −0.0180	−0.0083
15	+0.0714 +0.0334 +0.0334 +0.0327	+0.0907 −0.0001 −0.0001 +0.0134	+0.0013
15’	+0.0135 +0.0000 +0.0000 +0.0906	+0.0906 +0.0000 +0.0000 +0.0135	+0.0013
16	−0.0017 −0.0288 −0.0287 −0.0373	−0.0530 +0.0046 +0.0045 +0.0140	+0.0018
17	−0.0031 +0.0258 +0.0058 +0.0093	+0.0191 −0.0044 +0.0156 −0.0129	+0.0004
17’	−0.0074 +0.0232 +0.0033 +0.0136	+0.0190 −0.0156 +0.0043 −0.0128	+0.0004
18	−0.0019 −0.0332 −0.0332 −0.0277	−0.0436 −0.0210 −0.0210 +0.0140	−0.0006
19	+0.0001 +0.0155 +0.0155 +0.0180	+0.0270 +0.0000 +0.0000 −0.0089	+0.0001
20	+0.0032 −0.0064 −0.0064 −0.0042	−0.0076 −0.0021 −0.0021 +0.0066	+0.0013
20’	−0.0350 +0.0000 +0.0000 −0.0869	−0.0869 +0.0000 +0.0000 −0.0350	+0.0018

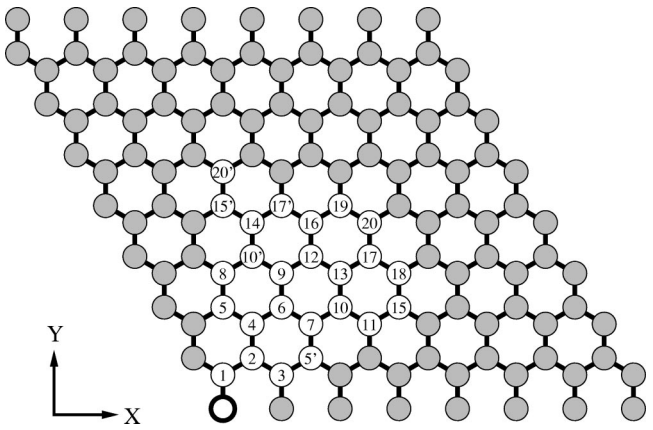

FIG. 5. Graphite single-layer supercell with the numbering scheme for the table of the force constants (Table II).

tial, any differences are a direct consequence of curvature effects and, hence, a good measure of their importance for the phonon dispersion.

The 4-times-replicated zigzag cell has the same height (17.0 Å) as the graphene super-cell in the y direction (Fig. 5). We expect that force constants beyond this range are zero. The height of the 4-times-replicated armchair supercell is smaller (9.8 Å); thus the dispersion relation for the (10,10)

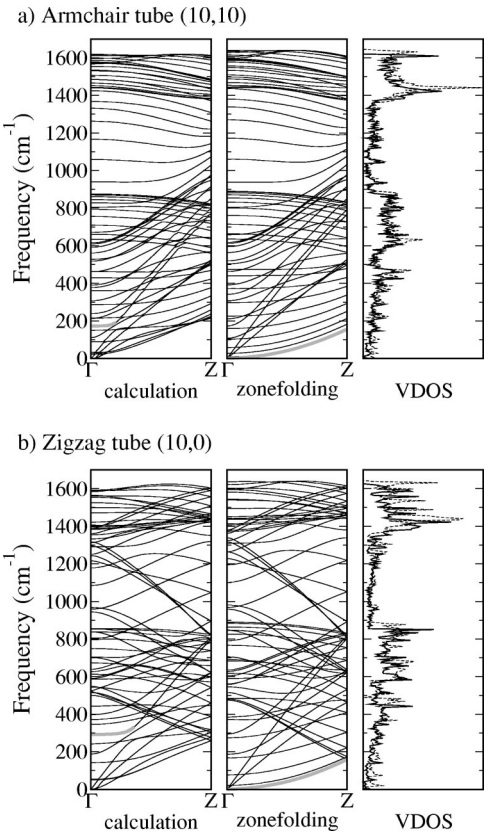

FIG. 6. Phonon dispersion relations and vibrational density of states for the armchair (10,10) and zigzag (10,0) tubes. Gray thick lines show branches of the radial breathing mode. The VDOS panels show the vibrational density of states for zone-folding (dashed line) and *ab initio* (solid line) calculations.

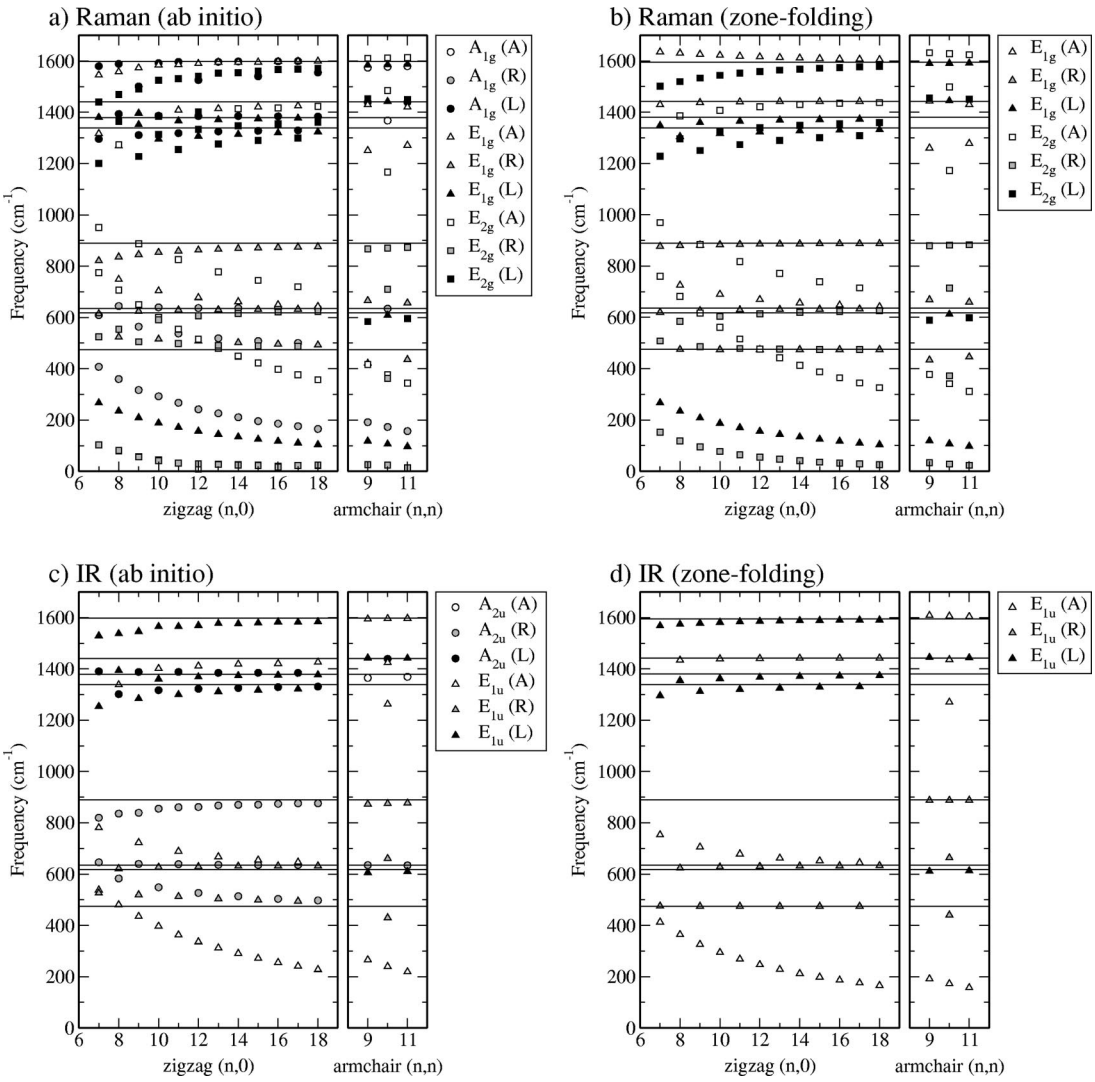

FIG. 7. Raman- and infrared-active modes (classified according to the symmetry representations). Panel (a) shows the calculated Raman frequencies and (b) the zone-folding Raman frequencies. Panels (c) and (d) display the calculated and zone-folding values for infrared-active frequencies, respectively. In all panels, horizontal lines indicate the zone-folding *A* mode frequencies. Letters A, R, and L indicate the direction of the vibration (Fig. 2): radial, axial, and longitudinal (parallel) to the tube axis.

tube might have somewhat larger error bars. Note that the Γ-point phonon frequencies do not depend on how often the cell is replicated.

As can be seen in Fig. 6, the agreement between *ab initio* and zone-folding calculations is remarkably good. The major difference between these two results is in the low-frequency part of the spectrum. The rise of the low-frequency phonon branches is slower in zone folding. The reason for this is a failure of the zone-folding approach to describe the branches of the radial breathing mode and the two translational modes perpendicular to the tube axis (x and y). In zone folding, the radial breathing mode is predicted to have zero frequency, while the two translational modes have finite frequency. Of course, the full *ab initio* calculations for nanotubes do not have this deficiencies.

Another difference, which is physically more interesting is a general softening of the *ab initio* modes compared to zone folding visible in the vibrational density of states of Fig. 6. This is caused mainly by a weakening of the interatomic forces due to curvature effects. The difference is around 3%, but the shift is not uniform among the frequencies. We discuss the differences between zone-folding and full *ab initio* calculations in more detail in the next section.

Figure 7 shows the frequencies of the Raman- and infrared-active modes identified according to the irreducible representations of the $D_n \otimes i$ group (D_{nd} for odd or D_{nh} for even n) (Ref. 34) and (Fig. 7). Modes were also classified by the direction in which the movement of atoms is most intense (Fig. 2): **R** (radial), perpendicular to the tube surface (e.g., radial breathing mode); **L** (longitudinal), parallel to the tube axis; **A** (axial), the direction perpendicular to radial and longitudinal (e.g., rotation around the tube axis). Let us first discuss zone folding. *A* modes are shown as straight lines in the two graphs for zone folding [Figs. 7(b) and 7(d)]. To guide the eye, these lines are also shown in the *ab initio* subpanels, and circles present the exact results for *A* modes. Since we present the Raman-active and IR-active modes in separate graphs, one usually finds circles that converge for

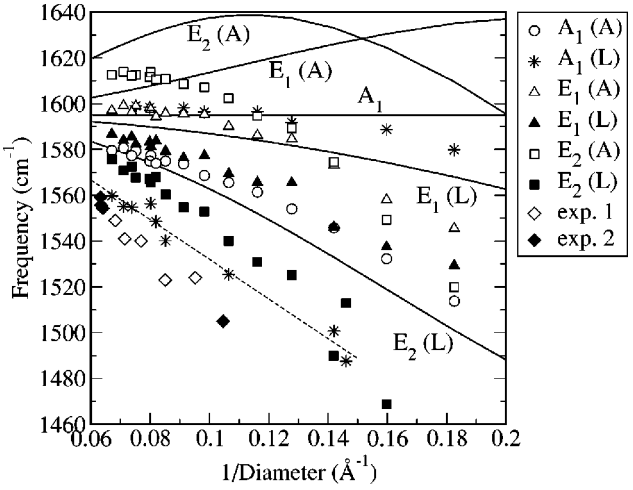

FIG. 8. Phonon frequencies in the *G* band calculated by *ab initio* density functional theory. Phonons are characterized by their symmetry and direction of vibration. Note that all A_1, E_1, and E_2 modes in the *G*-band region are shown irrespective of their parity. Experimental results for the frequency of the BWF line from Ref. 41 and Ref. 42 are shown by open and solid diamonds. Dashed line shows the linear fit for $A_1(L)$ mode in metallic tubes.

larger tubes towards the zone-folding value in one of the two graphs, (a) or (c). We however remind the reader that the A_{1u} modes are silent and, therefore, not shown in the graphs. Additionally some *A* modes with identical displacement patterns have either even or odd symmetry depending on whether *n* is even or odd. For instance, for the (18,0) tube, the $A_{2u}(R)$ (IR-active) mode at 495 cm^{-1} has the same displacement pattern as the $A_{1g}(R)$ (Raman-active) mode at roughly the same frequency for the (17,0) tube.

But in any case, deviations of circles from straight lines are indications for curvature effects. The curvature effect on other modes can be recognized by comparing the zone-folding and the *ab initio* panels. Clearly, curvature effects are rather small for all high-frequency modes. But a general softening is visible at smaller radii, leading to a decrease of the frequency of the $E_{1g}(A)$ (open triangles), $E_{1u}(L)$ (solid triangles), and $E_{2g}(L)$ (solid squares). The change is roughly 5% for the smallest tube considered here.

This is more clearly shown in Fig. 8, in which we concentrate on the *G*-band modes as a function of the inverse diameter (the same results as a function of the diameter were shown in Ref. 23). Since we have discussed most of the results already in Ref. 23, the following discussion is kept short. The zone-folding predictions are now shown as lines, with labels indicating their symmetry. Zone folding predicts a single *A* mode, a small splitting between the longitudinal and axial E_1 modes, and a slightly larger splitting between the two E_2 modes.[43] The splitting is not quite symmetric with respect to the central graphite frequency ω_g, since our force constants lead to a rather strong increase of the LO frequency from Γ to *M* (overbending) so that the average frequency is higher than for graphite. In Ref. 43 an average decrease of the frequencies was found with a different set of force constants fitted to experimental results.

The full *ab initio* calculations show a similar behavior, but some details are clearly different. Generally, the exact results are lower than the zone-folding values with the exception of the longitudinal $A_1(L)$ mode in insulating tubes (stars). The frequency shift with respect to zone folding is rather uniform and approximately 10 cm^{-1} for larger tubes. For the three largest tubes, the E_2 modes (squares) are now almost symmetrically split by approximately 20 cm^{-1} with respect to the central graphite frequency $\omega_g = 1595$ cm^{-1} (theory). These values compare well with recent polarized Raman studies of Jorio *et al.* where a symmetric splitting of the E_2 modes by 28 cm^{-1} was observed with respect to the experimental *G* band of graphite (experiment $\omega_g = 1580$ cm^{-1}).[44] However, experiments using parallel, crossed, and circularly polarized light find the E_2 modes overlapping in frequency with the A_1 modes.[45]

For large insulating tubes, the $E_1(A)$ modes and $A_1(L)$ modes (open triangles and stars) almost coincide and are located around 1597 cm^{-1}. The $E_1(L)$ and $A_1(A)$ modes (solid triangles and open circles) are also very close in frequency and found at roughly 1580 cm^{-1}, i.e., 20 cm^{-1} lower than the $E_1(A)$ and $A_1(L)$ modes. These values are also in reasonable agreement with Raman and polarized Raman studies,[43,44] where one E_1 and an A_1 mode were observed around 1590 cm^{-1}, and the other sets of E_1 and A_1 modes were observed at 1567 cm^{-1}.

The most interesting feature, however, is the significant drop of the frequency of the longitudinal $A_1(L)$ mode in metallic tubes compared to insulating tubes. The frequency drop is the same for zigzag, armchair, and chiral tubes with similar radii. For the linear fit of the frequency dependence on the inverse diameter $f(d) = f_0 - \alpha/d$ the parameters $f_0 = 1619$ cm^{-1} and $\alpha = 866$ cm^{-1} Å are obtained. A linear fit with the assumption that the frequency approaches 1595 cm^{-1} for $1/d \to 0$ yields $\alpha = 637$ cm^{-1} Å, but does not fit the theoretical results very satisfactory. This indicates a deviation from a simple linear behavior, also observed experimentally.[42]

We now return in our discussion to Fig. 7. For the intermediate frequencies around 800 cm^{-1} a similar softening as for the high-frequency modes is observed both for the Raman- and IR-active branches [$E_{1g}(R)$, gray triangle; $A_{2u}(R)$, gray circle]. At even lower frequencies (500 cm^{-1}) the differences between zone-folding and full *ab initio* calculations are generally larger and in the opposite direction. This part of the spectrum is dominated by vibrations in the (x,y) plane (radial and axial). Three modes show a peculiar behavior: the frequency dependence of the radial breathing mode [$A_{1g}(R)$, gray circles] exhibits the characteristic A/r scaling, where *r* is the tube radius and $A = 1144$ cm^{-1} Å, in good agreement with previous calculations using the same plane-wave code but different pseudopotentials (1170 cm^{-1} Å).[22] By fitting to Ar^{-B} we obtained the values $A = 1068$ cm^{-1} Å^B and $B = 0.95$. The value *B* is smaller than 1, which is due to the bond softening for narrower tubes. It has been emphasized that the $1/r$ behavior is a natural consequence of elastic continuum theory applied to nanotubes.[22]

TABLE III. Weighted average of angles between the displacement direction and the tube axis for selected phonon modes of the (12,6) tube. Weights are proportional to the displacement amplitude of each atom.

	Frequency (cm^{-1})	α (deg)
A_1(L)	1570	3.8
A_1(A)	1578	86.3
E_1(L)	1582	1.6
E_1(A)	1597	88.6
E_2(L)	1566	1.8
E_2(A)	1614	88.4

A second mode, which converges towards 495 cm^{-1} for large tubes, exhibits a similar behavior [gray circles in Figs. 7(a) and 7(c)]. For the tubes with even n, it has $A_{2u}(R)$ symmetry and is IR active, but for tubes with odd n it has $A_{1g}(R)$ symmetry and should be Raman active. Using the notation of Fig. 1 its displacements pattern is $++--$.

Finally we want to comment on the lowest-frequency mode observed below 100 cm^{-1} in the graphs for the Raman frequencies [Fig. 7(a)]. This mode is related to the ZA mode in graphite, which has a quadratic dispersion relation for $\vec{q} \rightarrow 0$, and hence approaches zero quadratically with increasing tube radius (at least in zone folding). In nanotubes, the mode causes a distortion from a circular to an elliptic shape. Our calculations show considerable noise in the frequency of this mode, which is related to error propagation that affects low-frequency modes much stronger than high-frequency modes. Nevertheless, it is clear that the frequency of that mode is substantially lower in the exact calculations than in zone folding. This possibly points to an instability of large nanotubes towards an elliptic deformation. However, up to the radii we have investigated here, all tubes remain stable towards such a deformation.

IV. DISCUSSION

A. Phonon eigenvectors

As discussed in the Sec. II D, the phonon modes of achiral nanotubes split into longitudinal and transversal modes, which might be further divided into radial and axial modes. Recently Reich *et al.*[45] pointed out that while in achiral tubes the inversion symmetry allows a division into longitudinal and transversal modes, in chiral tubes such a classification is meaningless. Since this might significantly alter the results for the mode softening, we performed test calculations on the metallic chiral (12,6) tube. As far as the mode softening is concerned we find similar results as for the achiral tubes (see also Fig. 1 of Ref. 23). Furthermore, the angle between the A_1, E_1, and E_2 modes and the tube axis was analyzed for the (12,6) nanotube. For this tube all totally symmetric modes (A_1) reasonably line up with the expected directions (deviations are less than 0.6°), with the exception of the longitudinal and axial G-band modes, which deviate by about 3.8° (Table III). For the E_1 and E_2 modes in the G band, the deviations are also tiny. Our calculations confirm the observation of Reich *et al.*, that symmetry does not require modes to be exactly longitudinal or transversal in chiral tubes, but for the particular tube we have considered, the deviations are smaller than reported by Reich *et al.* Thus a classification into longitudinal and transversal modes is still useful. Our tube is, however, wider than the ones considered by Reich *et al.*, and further studies are required to shed more light on this subject.

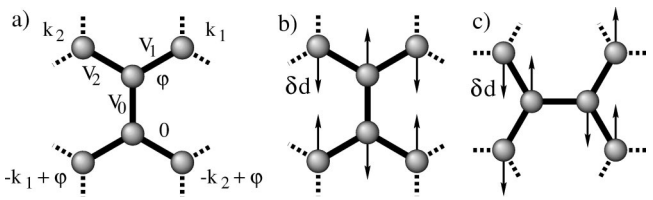

FIG. 9. (a) Conventions used in the tight-binding Hamiltonian. Displacement patterns of the longitudinal (axial) A_1 mode in (b) zigzag (armchair) and (c) armchair (zigzag) tubes. φ is the phase difference between the two carbon atoms in the unit cell (in rad/2π).

B. Mode softening

As shown in the previous section, in nanotubes, the vibrational frequencies are generally lower than one would expect on the basis of zone folding. This observation is not new, and all first-principles calculations agree that curvature lowers the interatomic force constants.[20] The effect is most likely related to a weaker π bonding in the circumferential direction in a curved graphite layer. This is also confirmed by the observation that the axial $A_1(A)$ mode is one of the modes that is most strongly affected by curvature, whereas (for semiconducting tubes) the longitudinal $A_1(L)$ mode is essentially independent of the radius (see Fig. 8).

The most important outcome of our calculations is, however, the large drop of the frequency of the longitudinal optic $A_1(L)$ mode in *all* metallic nanotubes (irrespective of their chirality). The corresponding displacement patterns of the $A_1(L)$ modes in zigzag and armchair tubes are indicated in Figs. 9(b) and 9(c). An A_1 mode with a similar frequency dependence is also observed experimentally in metallic nanotubes and well known for its peculiar Breit-Wigner-Fano line shape in Raman spectroscopy. Compared to graphite the frequency shift was observed to be proportional to the inverse diameter d of the tube, α/d, with $\alpha = 440$ cm^{-1} Å.[46] This is in reasonable agreement with our value of $\alpha = 637$ cm^{-1} Å. Visually, the agreement of the present density functional calculations with two more recent independent measurements is even better, as evidenced by Fig. 8.[41,42] The theoretical frequencies are roughly 10–20 cm^{-1} higher than the experimental ones, which corresponds to the discrepancy between theory and experiment for the LO mode in graphite. Such a discrepancy is therefore not unexpected. In Ref. 46, it has been suggested that the frequency drop is related to a coupling of the $A_1(A)$ modes to plasmons in metallic tubes. The coupling mechanism proposed in our recent theoretical work[23] also involves electronic states at the Fermi level. It is based on the observation that the $A_1(L)$

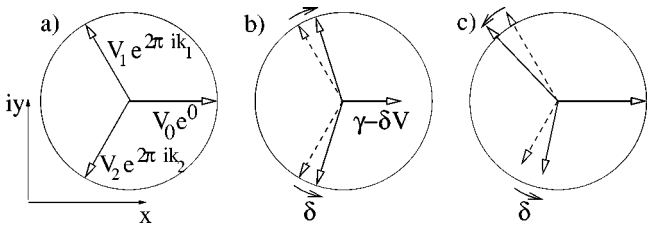

FIG. 10. Complex tight-binding matrix elements $V_i e^{2\pi i k_i}$ to the three neighboring atoms at the point in k space, where the two π bands cross each other (a) in undistorted graphite, $k_1=-k_2=1/3$, (b) for a longitudinal mode in zigzag tubes $k_1=-k_2=1/3-\delta$, and (c) for a longitudinal mode in armchair tubes $k_1=1/3+\delta$, $k_2=-1/3+\delta$. In all three cases, the three complex numbers sum to zero.

mode opens a gap at the Fermi level in all metallic tubes irrespective of chirality. This mechanism does not involve plasmons in the common sense, but both mechanisms have in common that they should yield roughly a $1/d$ shift of the A_1 mode compared to the LO mode of graphite, since in metallic tubes, the electronic density of states per carbon atom at the Fermi level is proportional to the inverse of the diameter. A more recent study of Jorio *et al.*,[42] however, observed a frequency shift proportional to $1/d^2$. Although our calculations also do not exhibit strictly a $1/d$ frequency shift, they deviate significantly from the suggested $1/d^2$ behavior. It is important to remark that in the diameter range of 10–16 Å covered in the present study, the data of Jorio *et al.* seem to agree with our results except for the mentioned constant error of 10 cm^{-1} (solid diamonds in Fig. 8). A $1/d^2$ shift is, at first sight, also not compatible with a coupling of plasmons to phonons. Further theoretical and experimental work is required in order to resolve this issue.

In the remainder of the section we will discuss the coupling mechanism between electronic states at the Fermi level and phonons. The discussion always refers to metallic tubes. Particular attention is devoted to symmetry considerations which are also relevant for a coupling between plasmons and phonons. An important outcome of this symmetry analysis is that only the $A_1(L)$ phonon can couple to the electronic continuum states at the Fermi level, which seems to suggest that an electron-phonon coupling cannot lower the $A_1(A)$ mode as assumed in the experimental work.[42,46]

Let us first make some simple considerations regarding the character of the wave functions at the Fermi level. In graphite, two bands cross the Fermi level at the K point.[47] The states have essentially p character with the p orbitals aligned normal to the tubule surface (π bonding). They can be described reasonably by a tight-binding Hamiltonian with zero on-site energy.[47] If only nearest-neighbor interactions are considered, the π Hamiltonian of a graphitelike system reduces to a simple 2×2 matrix

$$\begin{pmatrix} 0 & \text{compl.conjug.} \\ V_0+V_1e^{i2\pi k_1}+V_2e^{i2\pi k_2} & 0 \end{pmatrix}, \qquad (3)$$

where V_0, V_1, and V_2 are the tight-binding hopping matrix elements between nearest neighbors [compare Fig. 9(a)].

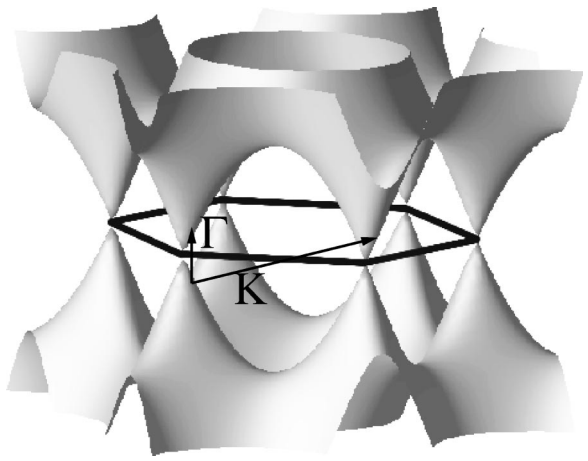

FIG. 11. Electronic band structure of graphite according to Eq. (3). The negative branch at lower energies corresponds to filled states, whereas the branch at energies higher than ϵ_F to empty states. Phonons that couple to the electronic states at the Fermi level are shown by arrows.

Here k_1 and k_2 are parametrizing the $\vec{k}$ point, with $\vec{k}=k_1\vec{b}_1-k_2\vec{b}_2$, where $\vec{b}_i$ are the reciprocal lattice vectors of the graphite plane. This Hamiltonian describes two bands that intersect at one particular point in the Brillouin zone.

Additionally, for a half-filled π band, as in the case of undoped graphite, the Fermi level is located exactly at the position where the two bands intersect. This band crossing point, where the Hamiltonian has one double-degenerated eigenvalue $\epsilon=0$, is determined by the requirement that the off-diagonal elements of the matrix become zero:

$$|V_0+V_1e^{i2\pi k_1}+V_2e^{i2\pi k_2}|=0. \qquad (4)$$

For a perfect graphene plane, $\gamma:=V_0=V_1=V_2$ holds due to symmetry, and the condition (4) is satisfied for $k_1=-k_2=\pm 1/3$, which corresponds to the K and K' points in graphite.[47,48] The graphical solution of condition (4) is illustrated in Fig. 10(a).

The two-dimensional band structure of graphite corresponding to Eq. (3) is shown in Fig. 11. Only a few phonons couple to the electronic states at the Fermi level. In linear response theory, the modifications resulting from a phonon κ are described by

$$\sum_{ij}(f_i-f_j)\frac{\langle\Psi_i|V_\kappa|\Psi_j\rangle}{(\epsilon_i-\epsilon_j)}, \qquad (5)$$

where Ψ_i and ϵ_i are the wave function and the eigenvalue corresponding to the one-electron state i, f_i is the number of electrons in this state ($f_i=0$ or $f_i=2$), and V_κ is the effective deformation potential corresponding to this particular phonon mode κ. If the occupied state has a Bloch wave vector k_i and the filled state a Bloch wave vector k_j, a finite coupling is only found, when the phonon wave vector is $q=k_i-k_j$; hence only Γ-point phonons and K-point phonons couple to the states at the Fermi level (see Fig. 11). In the present work, we are mainly interested in Raman-active modes. With the exception of $(3n,0)$ zigzag tubes, K-point

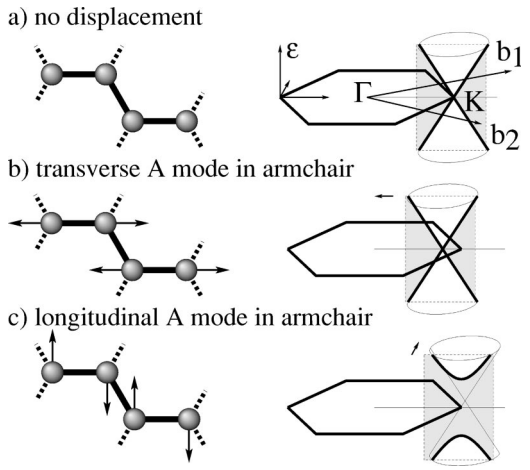

FIG. 12. (a) Electronic band structure of graphene in the vicinity of the *K* point. The bands have a conical shape near the *K* point, and the tip of the cone is located exactly at *K*. Panels (b) and (c) indicate the changes in the band structure for two phonon modes (LO and SH*). The thick lines indicate the band structure of an armchair tube, which is obtained by intersecting the gray plane with the two cones. Only the second displacement [corresponding to $A(L)$ in armchair tubes] opens a gap, whereas the first displacement only moves the intersection point.

phonons, generally, do not fold back to the Γ point, in nanotubes, as indicated in Fig. 3, and are not Raman active. Figure 3 also indicates that *K*-point phonons have E_n symmetry in $(3n,0)$ zigzag tubes, which implies that these modes are not Raman active for realistic wide tubes $(n>12)$.

Therefore, one can concentrate on Γ-point phonons. From the observation that the filled and unoccupied states in the vicinity of the Fermi level are orthogonal, it additionally follows that both atoms in the primitive cell of graphite must move in the opposite direction to result in a nonzero coupling element:

$$\langle \Psi_i | V_\kappa | \Psi_j \rangle = \int_\Omega \Psi_i(\mathbf{r}) \Psi_j^*(\mathbf{r}) V_\kappa(\mathbf{r}) d^3\mathbf{r}.$$

If the occupied and unoccupied states are in phase on one of the atoms, orthogonality of the wave functions Ψ_i and Ψ_j requires that they are out of phase on the second atom. Hence, for maximal coupling, the deformation potential must have an opposite sign on both atoms realized only by an out-of-phase movement of the two atoms in the primitive cell. Furthermore, in graphite, out-of-plane modes do not change the distance between neighboring atoms to first order, and therefore the hopping elements V_i remain unaffected to first order. Combining these three observations, we deduce that at the Γ point only the SH and LO modes of graphite couple to the electronic states at the Fermi level (one acoustic mode couples too, but this is not of relevance for the present study; see Ref. 49).

To study in detail, how the Γ-point SH and LO modes of graphite influence the band structure of graphite in the vicinity of the *K* point, we turn again to the graphical solution of Eq. (4). If the matrix element V_0 is decreased to $\gamma - \delta V$, which corresponds to the bond elongation shown in Fig. 9(b), the point where the bands intersect shifts away from *K* to $(1/3-\delta)(\vec{b}_1+\vec{b}_2)$ [Fig. 10(b)]. In the second case, corresponding to Fig. 9(c) and Fig. 10(c), one bond strengthens (V_1) and the second one weakens (V_2), leading to a shift of the crossing point to $(1/3+\delta)\vec{b}_1+(1/3-\delta)\vec{b}_2$.

How this affects the two-dimensional band structure of graphite is illustrated in Fig. 12. As already mentioned, two bands intersect at the *K* point (in fact there are two distinct points *K* and K', which cannot be linked by a reciprocal lattice vector, but for simplicity we will concentrate on one of these symmetry-inequivalent *K* points). For a pattern in which one bond is elongated, corresponding to the transverse mode in armchair tubes (and longitudinal mode in zigzag tubes), the crossing point shifts away from *K* towards Γ [Fig. 12(b)]. For the longitudinal mode in armchair tubes (and transverse mode in zigzag tubes), on the other hand, the crossing point moves perpendicular to the line ΓK [Fig. 12(c)].

The band structure of nanotubes near the Fermi level is obtained by the intersection of the two-dimensional band structure of graphene (cones) with those planes, which are allowed by the conditions imposed by the wrapping procedure.[50] For armchair tubes, the resulting band structure around ϵ_F is indicated in Fig. 12 using thick lines. The longitudinal mode opens a gap in the armchair tube, since the tip of the cones has moved perpendicular to the allowed lines, whereas the transverse mode leads only to a shift of k_F to a different *k* point. For the zigzag tubes, the arguments are similar, but the allowed lines are perpendicular to those for armchair tubes, and hence it is again the LO mode that opens the gap. In general, the displacement pattern, which moves the cone perpendicular to the lines that are allowed by the periodicity imposed by the wrapping procedure, will create the largest gap. This is in all cases the $A_1(L)$ mode, irrespective of chirality. Finally, it is important to emphasis that the gap opening is equally large for positive (dimerization) and negative (bond elongation) distortions. Hence the gap opens when the ions swing back and forth in a way compatible with the $A_1(L)$ mode.

At intermediate (electronic) temperatures the opening of the gap clearly reduces the energy, which is required to distort the nanotube by an amount roughly proportional to the square of the gap.[47,51] But it cannot eliminate the conventional restoring forces, stemming from the other parts of the electronic spectrum and from the direct interaction between the ionic cores. Thus the gap opening leads only to the mode softening and not to a permanent structure distortion. Since the density of states around ϵ_F is additionally inversely proportional to the radius of the tube, the $A_1(L)$ mode is softer for smaller tubes with a larger density of states at ϵ_F.[46] As an example for this process the band structure of distorted zigzag tubes was already presented in our previous work.[23]

Our final comment concerns the Raman activity of the $A_1(L)$ mode in metallic tubes. The Raman activity is related to the change of the polarizability. In a metallic tube, the screening is infinite for long-range charge fluctuations parallel to the tube, corresponding to an infinite polarizability parallel to the tube axes (compare Ref. 52). But any distortion of

the tube compatible to the $A_1(L)$ mode opens a gap and decreases the polarizability to a finite value. Hence the polarizability changes discontinuously for the $A_1(L)$ mode, which indicates an infinite Raman coupling tensor for this particular mode. Based on this simple argument we expect a very strong coupling of the $A_1(L)$ mode to incident light.

V. CONCLUSIONS

The first part of this work concentrated on the derivation of an accurate set of force constants for graphite. These force constants were calculated using *ab initio* density functional theory. We used this set of force constants to calculate the phonon dispersion relation of graphite and found reasonable agreement with experiment, although some notable discrepancies were observed in the vicinity of the *M* point. In particular, the theoretical SH mode has a too low frequency, and the theoretical frequency of the LA optic mode is somewhat too high compared to experiment. These discrepancies are difficult to reconcile with the fact that the agreement is almost perfect in the vicinity of the Γ and *K* points, suggesting that further experimental work might be required to fully resolve this issue. As an additional test for the reliability of the tabulated force constants, the elastic stiffness was calculated and compared to experiment. Again good agreement was found.

We then presented results for the vibrational properties of a large number of achiral nanotubes, calculated either using zone folding with the previously calculated force constants or using a full *ab initio* approach. Since all calculations relied on essentially the same potential and the same first-principles code, a direct assessment of how curvature affects the frequencies is possible. Our observations are similar to previous studies, insofar that we find a general softening of the high-frequency modes for small tubes. Qualitatively (and sometimes quantitative), the dispersion relations are, however, well described by the zone-folding approach. The exceptions are the known deficiencies in the low-frequency part of the vibrational spectrum.

Finally, we have analyzed in detail the behavior of the modes in the *G* band. In the *G* band, a general softening of all modes is again visible. The only exception is the $A_1(L)$ mode which is hardly influenced by curvature, since the bonds are not softened in the direction parallel to the tube. On the other hand, the $A_1(A)$ mode, having the same frequency as the $A_1(L)$ mode in graphite, softens considerably. Thus the splitting of these two modes is a good measure for the bond softening induced by curvature. The softening of $A_1(A)$ mode and a slight strengthening of $A_1(L)$ mode leads to the almost symmetric arrangement of $E_2(A)$, $E_1(A)+A_1(L)$, $E_1(L)+A_1(A)$, and $E_2(L)$ modes around the graphite *G* mode.

Finally, a significant softening of the $A_1(L)$ mode in metallic tubes is observed in our calculations. This is linked to a band gap opening at the Fermi level, a mechanism that is reminiscent of Peierls distortions. But here the gap opens when the ions swing back and forth from their ground-state position. The mechanism underlying this process is explained by means of a simple model based on a tight-binding Hamiltonian.

ACKNOWLEDGMENTS

This work was supported by the FWF under Grant No. P14095 and the EC network under Grant No. HPRN-CT-1999-00011.

[1] S. Ijima, Nature (London) **354**, 56 (1991).
[2] R. Al-Jishi and G. Dresselhaus, Phys. Rev. B **26**, 4514 (1982).
[3] R.A. Jishi, L. Venkataraman, M.S. Dresselhaus, and G. Dresselhaus, Chem. Phys. Lett. **209**, 77 (1993).
[4] R.A. Jishi, D. Inomata, K. Nakao, M.S. Dresselhaus, and G. Dresselhaus, J. Phys. Soc. Jpn. **63**, 2252 (1994).
[5] R.A. Jishi, L. Venkataraman, M.S. Dresselhaus, and G. Dresselhaus, Phys. Rev. B **51**, 11 176 (1995).
[6] P.C. Eklund, J.M. Holden, and R.A. Jishi, Carbon **33**, 959 (1995).
[7] R. Saito, T. Takeya, T. Kimura, G. Dresselhaus, and M.S. Dresselhaus, Phys. Rev. B **57**, 4145 (1998).
[8] A. Charlier, E. McRae, M.-F. Charlier, A. Spire, and S. Forster, Phys. Rev. B **57**, 6689 (1998).
[9] V.N. Popov, V.E. Van Doren, and M. Balkanski, Phys. Rev. B **59**, 8355 (1999); Solid State Commun. **114**, 395 (2000); Phys. Rev. B **61**, 3078 (2000).
[10] T. Aizawa, R. Souda, S. Otani, Y. Ishizawa, and C. Oshima, Phys. Rev. B **42**, 11 469 (1990).
[11] S. Siebentritt, R. Pues, K.-H. Rieder, and A.M. Shikin, Phys. Rev. B **55**, 7927 (1997).
[12] J. Yu, R.K. Kalia, and P. Vashishta, J. Chem. Phys. **103**, 6697 (1995).
[13] M. Menon, E. Richter, and K.R. Subbaswamy, J. Chem. Phys. **104**, 5875 (1996).
[14] C.T. White, D.H. Robertson, and J.W. Mintmire, Phys. Rev. B **47**, 5485 (1993).
[15] J.W. Mintmire and C.T. White, Carbon **33**, 893 (1995).
[16] D. Kahn and J.P. Lu, Phys. Rev. B **60**, 6535 (1999).
[17] R. Saito, A. Jorio, J.H. Hafner, C.M. Lieber, M. Hunter, T. McClure, G. Dresselhaus, and M.S. Dresselhaus, Phys. Rev. B **64**, 085312 (2001).
[18] P. Pavone, K. Karch, O. Schütt, W. Windl, D. Strauch, P. Giannozzi, and S. Baroni, Phys. Rev. B **48**, 3156 (1993).
[19] G. Kresse, J. Furthmüller, and J. Hafner, Europhys. Lett. **32**, 729 (1995).
[20] D. Sánchez-Portal, E. Artacho, J.M. Soler, A. Rubio, and P. Ordejón, Phys. Rev. B **59**, 12 678 (1999).
[21] C. Oshima, T. Aizawa, R. Souda, Y. Ishizawa, and Y. Sumiyoshi, Solid State Commun. **65**, 1601 (1988).
[22] J. Kürti, G. Kresse, and H. Kuzmany, Phys. Rev. B **58**, R8869 (1998).
[23] O. Dubay, G. Kresse, and H. Kuzmany, Phys. Rev. Lett. **88**, 235506 (2002).
[24] W. Kohn and L. Sham, Phys. Rev. **140**, A1133 (1965).

[25] R.O. Jones and O. Gunnarsson, Rev. Mod. Phys. **61**, 689 (1989).
[26] R. Car and M. Parrinello, Phys. Rev. Lett. **55**, 2471 (1985).
[27] M.C. Payne, M.P. Teter, D.C. Allan, T.A. Arias, and J.D. Joannopoulos, Rev. Mod. Phys. **64**, 1045 (1992).
[28] G. Kresse and J. Hafner, Phys. Rev. B **48**, 13 115 (1993).
[29] G. Kresse and J. Furthmüller, Comput. Mater. Sci. **6**, 15 (1996); Phys. Rev. B **54**, 11 169 (1996).
[30] P.E. Blöchl, Phys. Rev. B **50**, 17 953 (1994).
[31] G. Kresse and D. Joubert, Phys. Rev. B **59**, 1758 (1999).
[32] Y. Baskin and L. Mayer, Phys. Rev. **100**, 544 (1955).
[33] M. Methfessel and A.T. Paxton, Phys. Rev. B **40**, 3616 (1989).
[34] M.S. Dresselhaus, G. Dresselhaus, and R. Saito, Carbon **33**, 883 (1995).
[35] R.J. Nemanich, G. Lucovsky, and S.A. Solin, Mater. Sci. Eng. **31**, 157 (1977).
[36] F. Touinstra and J.L. Koenig, J. Chem. Phys. **53**, 1126 (1970).
[37] L.J. Brillson, E. Burstein, A.A. Maradudin, and T. Stark, in *The Physics of Semimetals and Narrow Gap Semiconductors*, edited by D.L. Carter and R.T. Bate (Pergamon, Oxford, 1971), p. 187.
[38] R.A. Friedel and G.C. Carlson, J. Phys. C **75**, 1149 (1971).
[39] P. Pavone, R. Bauer, K. Karch, O. Schütt, S. Vent, W. Windl, D. Strauch, S. Baroni, and S. de Gironcoli, Physica B **219& 220**, 439 (1996).
[40] D.H. Robertson, D.W. Brenner, and J.W. Mintmire, Phys. Rev. B **45**, 12 592 (1992).
[41] A. Kukovecz (unpublished); the tube diameters were determined as outlined in Ref. 53.
[42] A. Jorio, A.G. Souza Filho, G. Dresselhaus, M.S. Dresselhaus, A.K. Swan, M.S. Ünlü, B. Goldberg, M.A. Pimenta, J.H. Hafner, C.M. Lieber, and R. Saito, Phys. Rev. B **65**, 155412 (2002).
[43] A. Kasuya, Y. Sasaki, Y. Saito, K. Tohji, and Y. Nishina, Phys. Rev. Lett. **78**, 4434 (1997).
[44] A. Jorio, G. Dresselhaus, M.S. Dresselhaus, M. Souza, M.S.S. Dantas, M.A. Pimenta, A.M. Rao, R. Saito, C. Liu, and H.M. Cheng, Phys. Rev. Lett. **85**, 2617 (2000).
[45] S. Reich, C. Thomsen, G.S. Duesberg, and S. Roth, Phys. Rev. B **63**, 041401(R) (2001).
[46] S.D.M. Brown, A. Jorio, P. Corio, M.S. Dresselhaus, G. Dresselhaus, R. Saito, and K. Kneipp, Phys. Rev. B **63**, 155414 (2001).
[47] J.W. Mintmire, B.I. Dunlap, and C.T. White, Phys. Rev. Lett. **68**, 631 (1992).
[48] Noriaki Hamada, Shin-ichi Sawada, and Atsushi Oshiyama, Phys. Rev. Lett. **68**, 1579 (1992).
[49] M.T. Figge, M. Mostovoy, and J. Knoester, Phys. Rev. Lett. **86**, 4572 (2001).
[50] J.W. Mintmire and C.T. White, Phys. Rev. Lett. **81**, 2506 (1998).
[51] R.E. Peierls, *Quantum Theory of Solids* (Oxford University Press, New York, 1955), p. 108.
[52] L.X. Benedict, S.G. Louie, and M.L. Cohen, Phys. Rev. B **52**, 8541 (1995).
[53] H. Kuzmany, W. Plank, M. Hulman, Ch. Kramberger, A. Grüneis, Th. Pichler, H. Peterlik, H. Kataura, and Y. Achiba, Eur. Phys. J. B **22**, 307 (2001).